

Stochastic modeling of individual grain behavior during Ostwald ripening at ultra-high volume fractions of the coarsening phase

A. Spettl^{a,*}, T. Werz^b, C. E. Krill III^b, V. Schmidt^a

^a*Institute of Stochastics, Ulm University, Germany*

^b*Institute of Micro and Nanomaterials, Ulm University, Germany*

Abstract

The evolution of grains during coarsening phenomena like Ostwald ripening is a focus of recent and ongoing research. In the present paper, a new and flexible model is proposed that describes the statistical evolution of the “typical” individual grain size as a function of neighborhood characteristics. The grain size evolution (GSE) model defines a stochastic process based on contemporary mathematical techniques and requires only few (natural) assumptions. It is fitted to time-resolved experimental data of a semisolid Al–Cu alloy, in which the coarsening phase has an ultra-high volume fraction $V_V = 0.93$. Evaluation shows that the model describes the experimental data quite closely. The nature of this modeling approach serves to improve the understanding of coarsening processes at the intermediate level between coarsening mechanisms and global statistical properties. Furthermore, the model enables predictive simulations to be performed, based on an extension of an existing 3D microstructure model (Mod. Sim. Mat. Sci. Eng. 2015;23(6):065001) to 4D.

Keywords: spatiotemporal stochastic modeling, grain coarsening, Ostwald ripening, Gaussian copula, Laguerre tessellation

1. Introduction

Ostwald ripening is a process that occurs in multiphase systems, where particles (or droplets) of one phase are embedded in a matrix of one or more other phases. In order to minimize the excess energy contributed by interphase boundaries, large particles grow while small particles shrink and, ultimately, disappear. An introduction to Ostwald ripening and its experimental and theoretical investigation can be found in, *e.g.*, [1, 2, 3, 4, 5, 6], whereby the most important theoretical treatment of Ostwald ripening is the so-called LSW theory, presented by Lifshitz and Slyozov [7] as well as Wagner [8] in the early sixties. The latter describes the case of a vanishingly small volume fraction V_V of the coarsening phase, for which it is possible to treat every particle as an isolated object — *i.e.*, direct interactions between particles are not considered. The LSW theory predicts a power-law growth of the mean particle size (with exponent 3) and a particle size distribution whose shape does not change over time. In par-

ticular, the particle size distribution normalized to expectation unity is always the same distribution (statistical self-similarity [9]). However, the situation is more complicated for volume fractions V_V that are not near zero [10, 11, 12, 13, 14, 15], which has become a popular topic of recent research in the field. For example, experimental investigations [16, 17, 18, 19], analytical theories [20, 21] and large-scale computer simulations — based on, *e.g.*, phase-field and Monte-Carlo methods [22, 23, 24, 25] — have focused on volume fractions of technological relevance. Results suggest that the power-law growth and the self-similarity of particle size distributions still hold, although the shape of the particle size distribution changes at higher V_V [22, 24], and for $V_V > 0.9$ the power-law exponent may manifest a crossover to that of single-phase grain growth (exponent 2 at $V_V = 1.0$) [22]. However, convergence to steady-state conditions can be slow [26, 27].

The approaches mentioned above are all important for an improved understanding of the coarsening process. Yet, other (complementary) approaches have their merits, as well. For example, stochastic modeling of microstructures helps to identify the relevant structural characteristics of a given material, encompassing not

*Corresponding author

Email address: aaron.spettl@uni-ulm.de (A. Spettl)

only the average values of specific structural parameters but also their local fluctuations and spatial correlations. A stochastic 3D microstructure model for polycrystalline materials has been presented in [28], where the model was fitted to experimental data obtained for an Al-5 wt% Cu alloy heated to 592 °C. However, in [28] the dynamics of microstructural evolution were captured only at the statistical level but not for individual particles (hereafter referred to as *grains*). We aim to remedy this situation in the present paper. Our new treatment has several benefits. A stochastic description of individual grains and their evolution over time is useful to determine simple characteristics that influence (or, at least, are correlated with) the local evolution of grain sizes. The stochastic modeling approach proposed in the present paper can identify and account for such dependencies, while subsuming any additional, not-yet-identified factors influencing evolution to the “randomness” of the system. Note that stochastic models describing the evolution of grains have two important advantages. First, it is possible to identify (locally estimated) parameters of the microstructure that have a high impact on the local evolution. Second, predictive simulations are possible. As mentioned in [28], the latter is important for, *e.g.*, the multiscale computational models that are employed in Integrated Computational Materials Engineering (ICME) [29].

In this paper, we present a stochastic model that predicts changes in grain volume based on current grain size and characteristics of its neighborhood. More precisely, the model not only predicts the expected evolution of grain size but also its probability distribution — *i.e.*, the possible new grain sizes and their likelihoods. We call this model the *grain size evolution (GSE) model*. The latter is based on just a few assumptions — power-law growth [7, 8], self-similarity [7, 8, 9], temporal and spatial Markov property [30, 31] — and a further contemporary mathematical technique, the modeling of multivariate distributions with copulas [32, 33]. The GSE model describes the dynamical behavior of the “typical”¹ individual grain. In a second step, the 3D model for entire grain systems [28] is extended to 4D by integrating the GSE model.

We show the capability of the model to represent phe-

¹The terminology “typical grain” employed in the present paper conveys the following mathematical concept. Consider a grain ensemble, for which each grain has properties like size, shape, *etc.* For an unboundedly increasing number of such grains, these properties can all be described by probability distributions. Then, the typical grain is a random grain whose properties have these distributions, and, thus, the typical grain is representative of the entire grain system — see [34] for further details.

nomena observed in real materials by fitting it to time-resolved experimental data of a semisolid Al–Cu alloy, in which the coarsening phase occupies an ultra-high volume fraction ($V_V = 0.93$). These data were captured *in situ* with synchrotron X-ray tomography. It turns out that a large number of grains can be tracked, although the complexity of the image data renders it laborious to achieve high tracking efficiencies. Fortunately, even incomplete microstructural information suffices to establish the values of model parameters such that growth of individual grains is predicted quite accurately.

2. Experimental data, imaging and segmentation

In this section, the experimental sample, its time-resolved structural characterization, and image data processing are described.

2.1. Experimental sample and *in situ* 3D imaging

The experimental data considered here were drawn from the same measurements that were considered in [28]; however, now the time resolution of the data is exploited. Salient facts regarding sample preparation and 3D imaging are reviewed below.

An ingot of the alloy Al-5 wt% Cu was homogenized at 500 °C for 24 hours in air and subsequently cold-rolled to a thickness reduction of 50%. Cylindrical specimens — 8.5 mm in length and 4 mm in diameter — were cut from the rolled plate by spark erosion. A furnace was constructed to allow for time-resolved *in situ* tomographic characterization of such samples using X-ray radiation at beamline ID15A of the European Synchrotron Radiation Facility (ESRF). Over the course of 25 hours, a tomographic scan was recorded every 10 minutes while the specimen was held at 592 °C, which placed it in a semisolid state consisting of solid particles surrounded by a liquid matrix. Absorption-contrast tomography is able to distinguish between the particles and the matrix because the liquid absorbs X-rays more strongly than does the solid phase. This is due to the higher concentration of Cu dissolved in the matrix (22.4 wt% vs. only 3.5 wt% in the solid phase) at 592 °C. Application of the lever rule to the Al–Cu phase diagram [35] yields a volume fraction of the solid (coarsening) phase of $V_V = 0.93$ at thermodynamic equilibrium between the particles and the liquid matrix. The nominal resolution of the reconstructed tomographic data sets is given by the voxel side length of 5.36 μm .

We denote the 3D grayscale images obtained in this manner by $I_t = \{I_t(x, y, z) \in \{0, \dots, 255\} : (x, y, z) \in$

W }, where $W \subset \mathbb{N}^3$ is the grid of voxel coordinates, the grayscale values are in $\{0, \dots, 255\}$, and the annealing times $t \in T_{\text{exp}}$ belong to the set $T_{\text{exp}} = \{200, 210, \dots, 750\}$ (all specified in minutes). Note that the time span between two successive tomograms is always $t_{\text{step}} = 10$ minutes.

We make the same assumption as in [28] regarding steady-state conditions. We cannot be sure that the sample has actually reached the steady state by 200 minutes of annealing. Statistical characteristics (*e.g.*, the distributions of grain sizes and coordination numbers) seem to indicate the occurrence of self-similar coarsening [28], but it is still possible that the sample finds itself in a transient regime, the characteristics of which are evolving very slowly. In either event, it makes sense to fit a stochastic model to the experimental data, but in the transient case the stochastic model's predictive ability applies only to a limited extent beyond the time span at hand.

2.2. Identification of grains at fixed annealing times

In order to establish the parameters of the GSE model, we will require information regarding grain-size trajectories [19]. As a result, we must be able to recognize the same grain at subsequent or previous time steps, necessitating a consistent labeling of grains over the course of the measurements. The aim is to obtain a large number of trajectories, each of which extends over numerous time steps. In this section, we discuss the identification of individual grains within 3D data sets. These data form the basis for the tracking of grains across time steps, which we address in the following section.

Image processing was performed in a similar manner as in [28]. Ring artifacts were removed from grayscale data [36] (resulting image denoted by I_t), a global thresholding step was performed (binary image denoted by B_t), and a smoothing step was applied (resulting image denoted by B'_t). The main difference with respect to the image processing performed in [28] may be found in the identification of grains. We still employ a watershed transformation [37, 38, 39, 40], but instead of considering so-called *extended regional minima*, which we introduced in [28] to reduce the occurrence of oversegmentation, we now adopt the following simplified approach, which is computationally faster and therefore better suited to a large number of 3D data sets. For every local minimum, we can interpret the minimal distance to a grain boundary (*i.e.* the matrix phase) as the radius of a sphere centered at the local minimum. We then increase the radius of such a sphere by 10% and remove every other local minimum located within that

sphere that has a smaller minimal distance than the local minimum at the sphere center. This thinning of the set of local minima is very simple and reduces oversegmentation in many cases — *i.e.*, when the shape of the grains that are to be detected does not deviate too much from a spherical shape. (The deviations are the reason for the 10% radius increase.) The result of a marker-based watershed transformation [38, 41] applied to the thinned set of local minima is a binary image in which any holes in the network of grain boundaries have been filled in. This image is called B''_t . Finally, the same postprocessing was performed as in [28], yielding the image B'''_t . Every connected component in B'''_t corresponds to a single grain, which is assigned a unique label. The labeled image is specified by $L_t = \{L_t(x, y, z) \in \{0, \dots, N_t\} : (x, y, z) \in W\}$, where the value $L_t(x, y, z) \in \{1, \dots, N_t\}$ denotes the grain label, N_t is the total number of grains at time t , and $L_t(x, y, z) = 0$ corresponds to grain boundary regions (*i.e.* the matrix phase surrounding individual particles reduced to a thickness of one voxel). The grains themselves are given by $G_t(i) = \{(x, y, z) \in W : L_t(x, y, z) = i\}$, $i = 1, \dots, N_t$. The result is illustrated in Figure 1.

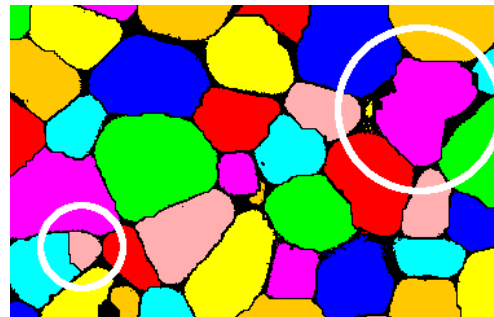


Figure 1: Planar section through a 3D tomographic data set, with identified grains assigned random colors. Examples for over- and undersegmentation are encircled in the bottom left and top right of the figure, respectively.

Note that regions of over- or undersegmentation remain. However, it is not necessary for the segmentation to be perfect (though this would, of course, be desirable). For any given point in time, the statistical information contained within the grain ensemble can be ascertained by the procedure outlined in [28], as it is feasible to achieve high quality in the segmentation of a single data set. In this paper, on the other hand, it is more important that the segmentation be highly consistent with respect to time. Segmentation errors reduce the length of grain trajectories, but for our purposes, the relevant fact is that the measured trajectories are reliable. The data sets are large enough to make

non-optimal tracking efficiencies acceptable. Note that there is no indication from a visual inspection of untracked grains that systematic bias has been introduced by the segmentation procedure: for example, the likelihood that a grain will be segmented properly appears to be independent of the particular grain's size class.

2.3. Extraction of grain trajectories

Finally, based on the labeled images L_t for all time steps $t \in T_{\text{exp}}$, grains must be tracked. A suitable method is proposed in [19], in which tracking is performed in reverse direction with respect to time. During the coarsening process, grains disappear over time, but no new grains nucleate. Therefore, every grain present at a given time $t \in T_{\text{exp}}$ must have existed at all times $t' < t$, as well. In particular, this is the case for the point in time that directly precedes t — namely, $t^- = t - t_{\text{step}}$. We assume that the prior grain region of $G_t(i)$ should be detected. First, possible grain candidates at time t^- are identified by detecting all grain regions $G_{t^-}(j)$, $j \in J \subset \{1, \dots, N_{t^-}\}$, that have their centroid voxel inside $G_t(i)$. Then, $G_{t^-}(j)$ is selected such that the best agreement in grain size is obtained. This is explained in the following. Denote by $r_{t^-}(j)$ the volume-equivalent radius of region $G_{t^-}(j)$, and by $r_t(i)$ the volume-equivalent radius of $G_t(i)$. For $j \in J$, the relative change is defined as $|r_t(i) - r_{t^-}(j)|/r_t(i)$. This relative change must lie below a threshold of $0.012 \bar{R}_t^2/r_t^2(i)$, where \bar{R}_t is the mean radius of all grains at time t . A central assumption is that a grain cannot change too much in only 10 minutes of annealing; the factor 0.012 has been selected manually (*i.e.*, it was lowered until no implausible jumps in grain sizes of trajectories were observed). If exactly one candidate $j \in J$ fulfills this criterion, the grain has been detected. Otherwise, either no grain is sufficiently close in volume to $r_t(i)$ or there is more than one candidate — in both cases, no tracking is performed. Note that this procedure reduces the impact of the relative change threshold, and in [19] the same methodology was shown to yield high grain tracking efficiencies for similar experimental data.

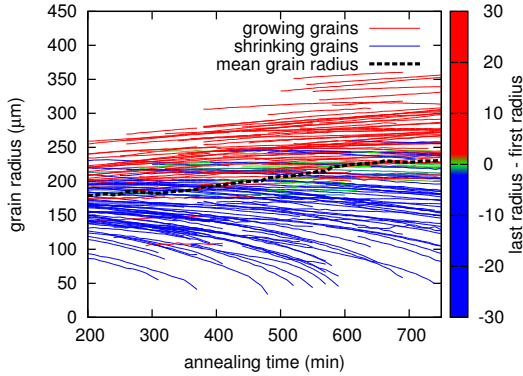
In this paper, the notation of grain trajectories is as follows. There are $M \in \mathbb{N}$ trajectories, where \mathbb{N} denotes the set of positive integers. Each trajectory $s(k)$, $k \in \{1, \dots, M\}$, is a time-indexed sequence of grain labels $\{l_k(t) \in \{1, \dots, N_t\} : t \in T_k\}$ where the trajectory is known at time points $T_k \subset T_{\text{exp}}$. The length $|s(k)|$ of a trajectory is given by the number $\#T_k > 0$ of elements in the set T_k . We allow incomplete information. Therefore, very often $T_k \neq T_{\text{exp}}$. Note that the tracking technique implies that the “death” of a grain is not observed, and the resulting trajectory with endpoint at non-zero grain

radius cannot be distinguished from a failure in tracking. It is clear that all time points in T_k must be sequential — time points in T_{exp} may be missing from T_k only before the beginning or after the end of a trajectory. (For example, if one grain is tracked for a long time, but with a single disruption in between, then it is represented as two separate grain trajectories.)

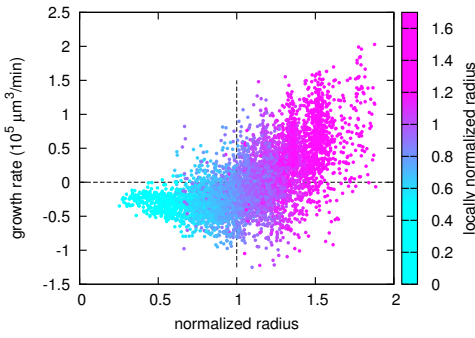
In the following analysis, an additional constraint is enforced: a trajectory must have a length of at least 12, *i.e.*, it can be tracked for at least 2 hours. This additional requirement helps to ensure the quality of trajectories, as it is unlikely for a long trajectory to be obtained by chance. Figure 2(a) shows trajectories of the volume-equivalent radii of experimental grains. Note that, as a matter of fact, trajectories are often incomplete, which means that there is no information for some time steps. Furthermore, if grains lie below a minimum size (below 25% of the mean radius), we assume that they are too small for tracking because their size changes more rapidly, and incorrect tracking would become increasingly likely. The experimental growth rates visualized in Figure 2(b) show the same qualitative behavior as in [19]. Note that the growth rates are computed from all observed transitions, *i.e.*, for all trajectories, every evolution in size is considered separately for two subsequent annealing times. The normalized radius is the volume-equivalent radius of a grain divided by the global mean radius at the respective point in time. Colors in Figure 2(b) indicate the values of locally normalized radii, *i.e.*, the grain radii relative to their respective local mean, *cf.* Section 2.4.

2.4. Local means

Similar as in [19], we consider a local mean radius of the neighborhood for every grain. We define the local mean radius as a weighted mean computed from all radii of adjacent grains. The weights are chosen as the square root of the respective grain–grain contact area in the watershed segmentation. Therefore, adjacency is defined as having a common face, *i.e.*, a positive value for the contact area of watershed basins (which is similar to the Voronoi cell construction proposed in [12] to determine relevant neighbors). Note that, usually, one would think of the standard (unweighted) mean or the contact area-weighted mean of all adjacent grains. However, the non-perfect segmentation of individual grains is a problem when evaluating local means (problematic grains are often small), and we obtained the best results by using “diameters” of contact areas as weights. Nonetheless, we take additional steps to improve the reliability of the data.



(a) Size trajectories of experimental grains. Note that experimental trajectories are detected only as long as grains are above a predefined minimum size. The color of a trajectory indicates the difference in endpoint radii.



(b) Volumetric growth rates $4\pi r_t^2(i)(r_{t^+}(j) - r_t(i))/(t^+ - t)$ obtained from experimental grain radius transitions $r_t(i)$ to $r_{t^+}(j)$, where grain i at time t belongs to the same trajectory as grain j at time t^+ ; for all trajectories $s(k)$, $k \in \{1, \dots, M\}$, and for all $t \in T_{\text{exp}}$, $t^+ = t + t_{\text{step}} \in T_{\text{exp}}$. Normalized radii are computed at time t .

Figure 2: Experimental trajectories of grain sizes and volumetric growth rates. (For purposes of visualization, only a subset of all trajectories is shown.)

First, a moving-average procedure is applied to the local means. For a given grain at a certain time, the (smoothed) local mean is computed by averaging over 5 local means, namely, besides the local mean of the given time step, the two local means of the two previous time steps and the two subsequent time steps (if present). This is reasonable as the local mean should not change too much in a short time span. Then, in a second step, a grain trajectory is rejected if the corresponding local mean value changes suddenly (in spite of the moving average smoothing), *i.e.*, if the difference of two subsequent local mean values is larger than 2% of the global mean. In these cases, there are problems in the neighborhood and it is better to ignore such data

altogether.

The grain radius relative to the local mean is shown with the help of colors for grain growth rates in Figure 2(b). This ratio is called the *locally* normalized radius in this paper; the term “normalized radius” without this emphasis refers to the usual normalization with the global mean (*cf.* \bar{R}_t , Appendix B). The colors indicating the locally normalized radii correspond roughly to the (globally) normalized radii, as it is likely for grains that are large (small) with respect to the global mean to be large (small) with respect to the local mean, as well.

3. The grain size evolution model

The proposed GSE model is essentially a stochastic process that describes the dynamical behavior of the “typical” (*cf.* footnote¹) single grain — where, in particular, its size is of interest. The interpretation of the notion of the “typical grain” is that one looks at a random grain in the (large) ensemble of grains at some initial time, *e.g.*, $t = 0$, which has the random (non-deterministic) volume-equivalent radius R_0 . We assume that there is a stochastic process $\{\hat{R}_t, t \geq 0\}$ with $\hat{R}_0 = R_0$, where the random variables \hat{R}_t correspond to the radii of the typical grain at annealing times $t > 0$. If the grain vanishes, its radius is defined to be zero (and a grain having radius zero may never “jump” to a positive radius again). Note that the possibility of having a radius of zero is the reason for the notation \hat{R}_t (instead of R_t without ring). If we want to consider the radius under the condition that the typical grain is “alive” at time t , we write R_t where $R_t = (\hat{R}_t | \hat{R}_t > 0)$.

For simplicity, only discrete and equidistant time steps are considered. In particular, the random variables $\{\hat{R}_t, t \in T_{\text{model}}\}$ should be described by a model, and the set of time steps is assumed to be $T_{\text{model}} = \{t_{\text{min}}, t_{\text{min}} + t_{\text{step}}, t_{\text{min}} + 2t_{\text{step}}, \dots\}$ for some $t_{\text{min}} \geq 0$ and $t_{\text{step}} > 0$. Note that we may opt to choose the typical grain from all grains at some annealing time $t_{\text{min}} > 0$ instead of $t_{\text{min}} = 0$, and consider the evolution starting from that point in time. Later on, simulation is stopped at time t_{max} , *i.e.*, we set $T_{\text{sim}} = \{t \in T_{\text{model}} : t \leq t_{\text{max}}\} = \{t_{\text{min}}, \dots, t_{\text{max}}\}$. We assume that $\hat{R}_{t_{\text{min}}} > 0$ with probability one, *i.e.*, only grains that exist at time t_{min} are considered.

In principle, the family $\{\hat{R}_t, t \in T_{\text{sim}}\}$ of finitely many random variables could be interpreted as a random vector with dimension $\#T_{\text{sim}}$. Such a random vector is described by its multivariate (joint) distribution. However, assuming a so-called Markov property it suffices to con-

sider the pairs

$$(\dot{R}_{t_{\min}+i t_{\text{step}}}, \dot{R}_{t_{\min}+(i+1)t_{\text{step}}}), \quad i = 0, 1, \dots,$$

which is significantly easier. The assumption is that the evolution of grains from time t to $t^+ = t + t_{\text{step}}$ does not depend on the earlier history, *i.e.*, the grain trajectory up to the time step immediately before t .² This type of assumption is called the Markov property, and it can be properly defined using the theory of stochastic processes — see, *e.g.*, [30]. With this assumption, the GSE model needs only to describe the transitions from a discrete point in time $t \in T_{\text{model}}$ to the next point in time t^+ — without any knowledge of its state at previous time points. If the distributions of all pairs $(\dot{R}_t, \dot{R}_{t^+})$ are known for all $t \in T_{\text{model}}$, then a trajectory $\{r_{t_{\min}}, \dots, r_{t_{\max}}\}$ of radii of the typical grain can be simulated. First, a realization of the typical grain radius at time t_{\min} is obtained, *i.e.*,

$$r_{t_{\min}} \sim \dot{R}_{t_{\min}}.$$

Then, the radii of subsequent time steps are obtained iteratively by conditional sampling, *i.e.*,

$$\begin{aligned} r_{t_{\min}+t_{\text{step}}} &\sim (\dot{R}_{t_{\min}+t_{\text{step}}} \mid \dot{R}_{t_{\min}} = r_{t_{\min}}), \\ r_{t_{\min}+2t_{\text{step}}} &\sim (\dot{R}_{t_{\min}+2t_{\text{step}}} \mid \dot{R}_{t_{\min}+t_{\text{step}}} = r_{t_{\min}+t_{\text{step}}}), \\ &\vdots \\ r_{t_{\max}} &\sim (\dot{R}_{t_{\max}} \mid \dot{R}_{t_{\max}-t_{\text{step}}} = r_{t_{\max}-t_{\text{step}}}). \end{aligned}$$

A second assumption is very important for the construction of the model. A widely accepted belief for grain coarsening phenomena like Ostwald ripening is self-similarity of the particle size distribution [9]. We give a short definition. Suppose \bar{R}_t returns the expected grain radius of the observable (*i.e.*, non-dead) grains for every time $t \geq 0$, *e.g.*, it is given by the power-law growth formula, see formula (B.1) in the appendix. Let $\{X_t, t \geq 0\}$ denote a time-indexed family of non-negative random variables with (cumulative) distribution functions $F_t(x) = \mathbb{P}(X_t \leq x)$, $x \geq 0$, for all $t \geq 0$. We

²Note that our aim is not to obtain a model that predicts future grain size evolution based on some kind of “fit” to past behavior; rather, we seek a model that bases its predictions solely on the current state of the microstructure, as is the case for the physical system. (All driving forces for coarsening follow entirely from the current state of boundary curvatures, concentration gradients and other microstructural parameters.) Within the context of our modeling approach, our goal is to reduce the degree of “randomness” in a single transition (*i.e.* to improve the prediction) by considering additional (local) microstructure characteristics that influence coarsening behavior. We then treat any remaining randomness as a random walk (Markov assumption).

call $\{X_t, t \geq 0\}$ or $\{F_t, t \geq 0\}$ self-similar (with respect to $\{\bar{R}_t, t \geq 0\}$) if the relationship

$$F_t(y \bar{R}_t) = F_0(y \bar{R}_0), \quad y \geq 0,$$

holds for all $t > 0$. Now, recall that $R_t = (\dot{R}_t \mid \dot{R}_t > 0)$, *i.e.*, radii of dead grains are excluded in R_t . Then, the assumption is that the distribution functions $\{F_{R_t}, t \in T_{\text{model}}\}$ of the time-dependent radii $\{R_t, t \in T_{\text{model}}\}$ for the typical (non-dead) grain are self similar.

3.1. Modeling the marginal distributions

Recall that we want to describe the bivariate distribution of the random vector $(\dot{R}_t, \dot{R}_{t^+})$ for all $t \in T_{\text{model}}$. By modeling these bivariate distributions, the stochastic GSE model is obtained. We propose to use copula-based probability distributions, for which a short introduction can be found in Appendix A. A big advantage of this approach is that one can describe the marginal distributions of \dot{R}_t and \dot{R}_{t^+} separately, and the copula itself is a special bivariate distribution function that describes the dependency between the two components \dot{R}_t and \dot{R}_{t^+} .

Therefore, first, we consider the marginal distributions of the vector $(\dot{R}_t, \dot{R}_{t^+})$. Obviously, owing to the definition of R_t , \dot{R}_t is exactly R_t if $\dot{R}_t > 0$, and otherwise $\dot{R}_t = 0$. The event $\dot{R}_t = 0$ occurs with a particular probability $q_t \in [0, 1]$. Consequently, the distribution of \dot{R}_t is given by a weighted mixture of R_t (with distribution function F_{R_t}) and “dead” grains (described by a degenerate distribution that assigns all mass to radius zero), whereby the weighting factor q_t denotes the proportion of grains at time t that have died. In other words, the distribution function of \dot{R}_t is given by

$$F_{\dot{R}_t}(x) = (1 - q_t) F_{R_t}(x) + q_t \mathbb{1}\{x \geq 0\}, \quad x \geq 0, \quad (1)$$

where $\mathbb{1}\{x \geq 0\}$ is the radius distribution function of dead grains, *i.e.*, it is equal to unity for $x \geq 0$. The quantity q_t clearly depends on t and on the first considered point in time, *i.e.*, t_{\min} , which we assume to be fixed. In particular, note that $q_{t_{\min}} = 0$.

Analogously to \dot{R}_t , the distribution of \dot{R}_{t^+} has the same decomposition as given in (1) (with R_{t^+} and q_{t^+}). Note that the distributions of R_t and R_{t^+} are assumed to be self-similar with respect to $\{\bar{R}_t, t \geq 0\}$, *i.e.*, $F_{R_t}(y \bar{R}_t) = F_{R_{t^+}}(y \bar{R}_{t^+})$ for all $y \geq 0$. Furthermore, because grains do not nucleate, $\dot{R}_{t^+} = 0$ must hold with probability 1 if $\dot{R}_t = 0$. This implies $q_t \leq q_{t^+}$.

Now, at this point, the question is: is it necessary to choose q_t , $t \in T_{\text{model}}$, as a certain value to be consistent with natural conditions to the model? It turns out that

470 the answer is yes. First, recall that $\mathring{R}_{t_{\min}} = R_{t_{\min}}$ by definition, *i.e.*, the typical grain selected at starting time t_{\min} is not a dead grain.

Simply as a tool to obtain q_t , we look at the random vector $(\mathring{R}_{t_{\min}}, \mathring{R}_t)$ because we know that $q_{t_{\min}} = 0$. Therefore, by (1), the marginal distribution functions of the random vector $(\mathring{R}_{t_{\min}}, \mathring{R}_t)$ are given by

$$\begin{aligned} F_{\mathring{R}_{t_{\min}}}(x) &= F_{R_{t_{\min}}}(x), & x \geq 0, \\ F_{\mathring{R}_t}(x) &= (1 - q_t) F_{R_t}(x) + q_t, & x \geq 0. \end{aligned} \quad (2)$$

480 It is known how the expectation of the grain radius distribution evolves with time. Furthermore, it is clear that the total volume of a set of grains must not change over time. Growing grains gain volume from shrinking grains — but in total, no volume may be lost or added in this process (*i.e.*, mass conservation is assumed). Therefore, a natural requirement is that the expected volume remain constant — *i.e.*,

$$485 \int_0^\infty x^3 dF_{\mathring{R}_{t_{\min}}}(x) = \int_0^\infty x^3 dF_{\mathring{R}_t}(x). \quad (3)$$

Note that dead grains with volume zero are included on the right-hand side, and their former volume is available to other grains. Now, q_t can be evaluated by combining (2) and (3). First, it holds that the left-hand side of (3) can be rewritten as

$$\begin{aligned} \int_0^\infty x^3 dF_{\mathring{R}_{t_{\min}}}(x) &= \int_0^\infty x^3 dF_{R_{t_{\min}}}(x) \\ &= \bar{R}_{t_{\min}}^3 \int_0^\infty y^3 dF_{R_{t_{\min}}}(y\bar{R}_{t_{\min}}), \end{aligned} \quad (4)$$

and the right-hand side of (3) is given by

$$\begin{aligned} \int_0^\infty x^3 dF_{\mathring{R}_t}(x) &= (1 - q_t) \int_0^\infty x^3 dF_{R_t}(x) \\ &= (1 - q_t) \bar{R}_t^3 \int_0^\infty y^3 dF_{R_t}(y\bar{R}_t). \end{aligned} \quad (5)$$

Therefore, (3) is equivalent to

$$\begin{aligned} \bar{R}_{t_{\min}}^3 \int_0^\infty y^3 dF_{R_{t_{\min}}}(y\bar{R}_{t_{\min}}) &= (1 - q_t) \bar{R}_t^3 \int_0^\infty y^3 dF_{R_t}(y\bar{R}_t) \\ \Leftrightarrow \bar{R}_{t_{\min}}^3 \int_0^\infty y^3 dF_{R_0}(y\bar{R}_0) &= (1 - q_t) \bar{R}_t^3 \int_0^\infty y^3 dF_{R_0}(y\bar{R}_0) \\ \Leftrightarrow \bar{R}_{t_{\min}}^3 &= (1 - q_t) \bar{R}_t^3 \\ \Leftrightarrow q_t &= 1 - \bar{R}_{t_{\min}}^3 / \bar{R}_t^3, \end{aligned} \quad (6)$$

490 where the first equivalence holds because of the self-similarity of $\{F_{R_t}, t \in T_{\text{model}}\}$ — *i.e.*, the variable of integration y denotes the normalized radius and $F_{R_t}(y\bar{R}_t) =$

$F_{R_0}(y\bar{R}_0)$ for $y \geq 0$. Obviously, $q_t \in [0, 1]$ holds because $\bar{R}_t \geq \bar{R}_{t_{\min}}$ for $t \geq t_{\min}$.

In this section, the marginal distributions of $(\mathring{R}_t, \mathring{R}_{t^+})$ have been described, and the required probability q_t of a grain to vanish in the time interval $(t_{\min}, t]$ has been determined. However, the copula capturing the dependence structure still has to be specified.

3.2. Co-monotonicity copula

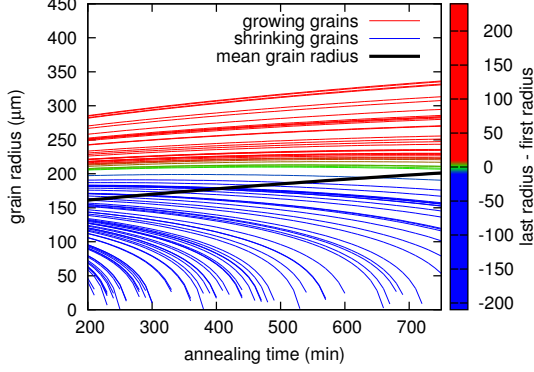
For an easier understanding of the modeling approach, we first plug in the co-monotonicity copula C^+ (which, to begin with, has no parameters, see Appendix A) and simulate grain trajectories. The marginal distributions of R_t , $t \in T_{\text{model}}$ are chosen by using parameter values obtained from the fitted model presented in [28] (see also Appendix B). There is a close relationship between seed point radii and grain radii, see [28], therefore we simply set $R_t \sim \mathcal{N}_+(c_\mu \bar{R}_t, c_\sigma^2 \bar{R}_t^2)$ (*i.e.*, the normal distribution with expectation $c_\mu \bar{R}_t$ and standard deviation $c_\sigma \bar{R}_t$, truncated to the interval $(0, \infty)$). The values of the parameters $c_\mu > 0$, $c_\sigma > 0$ and the specification of the power-law growth formula (B.1) are given in Appendix B. For $t \in T_{\text{model}}$, $t^+ = t + t_{\text{step}}$, the bivariate distribution of $(\mathring{R}_t, \mathring{R}_{t^+})$ is assumed to be given by

$$F_{(\mathring{R}_t, \mathring{R}_{t^+})}(x_1, x_2) = C^+(F_{\mathring{R}_t}(x_1), F_{\mathring{R}_{t^+}}(x_2)), \quad (7)$$

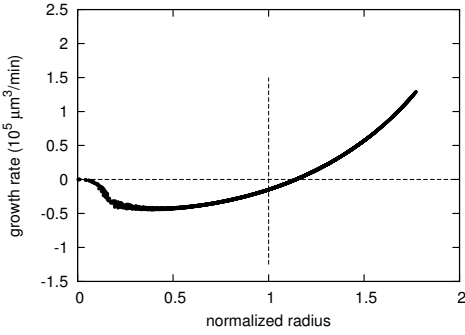
for $x_1, x_2 \geq 0$, where both marginal distribution functions are defined as given in (1). Note that x_1, x_2 are the grain radii at time t and t^+ , respectively, and the distribution function given in (4) specifies their relationship. However, this equation does not directly describe the evolution from x_1 to x_2 ; rather, loosely speaking, it essentially specifies how often x_1 and x_2 can occur together. The co-monotonicity copula ensures that $\mathring{R}_{t^+} = 0$ holds almost surely (*i.e.*, with probability 1) if $\mathring{R}_t = 0$. For the co-monotonicity copula, this is equivalent to $q_t \leq q_{t^+}$, which is obviously fulfilled.

Figure 3(a) shows the trajectories of 100 simulated grains. Note that the initial radii of grains are random, but the evolution is deterministic (because the co-monotonicity copula implements a perfect, deterministic dependence). It can be observed that, in principle, the simulated grain evolution exhibits the same behavior as found in experimental data, *cf.*, Figure 2(a), or Figure 9 in [19]. Furthermore, Figure 3(b) shows growth rates determined from simulated grain radius transitions. A very good qualitative agreement with the polynomial fit curve in Figure 10 of [19] can be observed. The behavior for very small grain radii is surprising at a first glance, but it can be explained: the grain radius shrinks quickly, but the (squared) absolute grain

radius is already very small, causing the growth rate to tend toward zero.



(a) Size trajectories of simulated grains. (The transition to radius zero is not drawn because the slope would change suddenly due to the discreteness of the time steps.)



(b) Volumetric growth rates $4\pi r_t^2(r_{t^+} - r_t)/t_{\text{step}}$ obtained from grain radius transitions r_t to r_{t^+} in all simulated trajectories, for $t \in T_{\text{sim}}$ and $t^+ = t + t_{\text{step}} \in T_{\text{sim}}$.

Figure 3: Simulation results for 2D GSE model with co-monotonicity copula and parameters from [28].

At this point, we note that this simple example with the co-monotonicity copula corresponds to the expected behavior of grains when only the global mean radius is used as a criterion for evolution. Two trajectories starting from different initial radii (at the same time) will never intersect. Such idealized “globally driven” coarsening is interesting in its own right, although it cannot be investigated experimentally (for high volume fractions of the coarsening phase). By using another copula type, it is possible to introduce randomness into the individual transitions, which is closer to the experimental situation. For this reason, the Gaussian copula (*cf.* Appendix A) will be used in the remainder of the paper. Note, however, that the Gaussian copula is but the simplest possible choice — in Section 4.2, we will give reasons why another copula may better be able to describe

experimental coarsening data.

3.3. Parametric model with Gaussian copula

Instead of the co-monotonicity copula used as a first trial in the previous section, a Gaussian copula is applied now. The bivariate Gaussian copula $C_{\Sigma}^{\text{Gauss}} : [0, 1]^2 \rightarrow [0, 1]$ has a correlation matrix of the form

$$\Sigma = \begin{pmatrix} 1 & \rho \\ \rho & 1 \end{pmatrix},$$

where $\rho \in [-1, 1]$ controls the correlation strength. For simplicity, we call ρ the correlation coefficient (even though it does not need to correspond to the (Pearson) correlation coefficient of the constructed distribution). The correlation may be time-dependent; however, just for this example, we take the correlation coefficient to be constant.

A direct (but unfortunately incorrect) approach would be to use the Gaussian copula by setting

$$F_{(\hat{R}_t, \hat{R}_{t^+})}(x_1, x_2) = C_{\Sigma}^{\text{Gauss}}(F_{\hat{R}_t}(x_1), F_{\hat{R}_{t^+}}(x_2)), \quad x_1, x_2 \geq 0.$$

This is problematic owing to the existence of vanishing grains, as the Gaussian copula does not ensure that $\hat{R}_{t^+} = 0$ holds almost surely if $\hat{R}_t = 0$. (Recall that the density of normal distributions is strictly positive. In particular, here, the first radius $x_1 = F_{\hat{R}_t}^{-1}(u_1)$ is zero for $u_1 \in [0, q_t]$, and the second radius $x_2 = F_{\hat{R}_{t^+}}^{-1}(u_2)$ is non-zero for $u_2 \in [q_{t^+}, 1]$, and integrating the Gaussian copula density over the area $[0, q_t] \times [q_{t^+}, 1]$ yields a positive probability.)

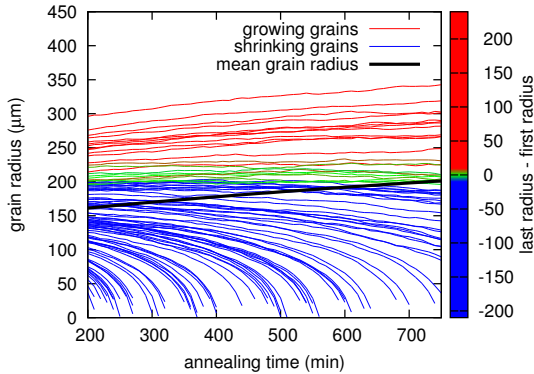
Therefore, we make use of the ordinal sum copula construction (see Appendix A). We use the independence copula C^{II} as the “lower part” C_1 and the Gaussian copula $C_{\Sigma}^{\text{Gauss}}$ as the “upper part” C_2 for the ordinal sum. The threshold h is chosen as q_t , the resulting ordinal sum copula is denoted by C_{q_t} . Then, the joint distribution of $(\hat{R}_t, \hat{R}_{t^+})$ is given by

$$F_{(\hat{R}_t, \hat{R}_{t^+})}(x_1, x_2) = C_{q_t}(F_{\hat{R}_t}(x_1), F_{\hat{R}_{t^+}}(x_2)), \quad x_1, x_2 \geq 0.$$

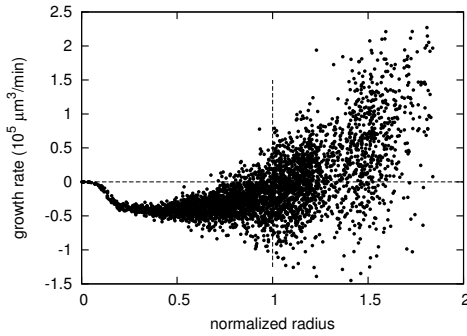
This way it is ensured that a radius of zero at time t is always mapped to radius zero at time t^+ (because integrating the ordinal sum copula density over the area $[0, q_t] \times [q_{t^+}, 1]$ yields zero). Note that C_1 could be any copula — the ordinal sum construction itself is sufficient to obtain this absorption property of radius zero.

To assess the effect of the randomness in transitions, we simulated grain trajectories for a Gaussian copula with a very high correlation of $\rho = 0.99995$. Note that conditional samples can be obtained quite easily from

a Gaussian copula — see, *e.g.*, [33]. As can be seen in Figure 4, the randomness of a transition is clearly visible. The volumetric growth rates scatter and do not follow exactly the curve in Figure 3(b). With such a model it is possible for trajectories to intersect, *i.e.*, two grains with the same size may evolve differently.



(a) Size trajectories of simulated grains.



(b) Volumetric growth rates $4\pi r_t^2(r_{t^+} - r_t)/t_{\text{step}}$ obtained from grain radius transitions r_t to r_{t^+} in all simulated trajectories, for $t \in T_{\text{sim}}$ and $t^+ = t + t_{\text{step}} \in T_{\text{sim}}$.

Figure 4: Simulation results for 2D GSE model with Gaussian copula, correlation coefficient $\rho = 0.99995$ and parameters from [28].

3.4. Extension to neighborhood description

In the previous section, the deviation of the grain evolution from the expected behavior was modeled by a non-deterministic dependence on time. However, one would really like to explain these deviations by other characteristics. It is very likely that the neighborhood of grains influences their evolution. For example, in [19], grain radii are considered that are normalized by a local mean instead of the global mean radius. We implement neighborhood characteristics as an additional component to our GSE model, by extending it from two to (in this case) four dimensions.

Such a dependence on (only) some kind of neighborhood in the modeling is essentially equivalent to the assumption of a spatial Markov property — *i.e.*, a certain conditional independence is assumed. Suppose we have a graph whose vertices are random variables describing radii of grains and whose edges represent the neighborhood structure of grains. Then, the *local Markov property* is fulfilled if the radius of any given grain is independent of all other random variables, given the radii of its neighbors. This concept is known from the theory of Markov random fields (also called Markov networks), which in turn are a generalization of the Ising model — see, *e.g.*, [31, 42, 43].

Suppose we have some local mean radius \bar{R}_t^{local} , $t \in T_{\text{model}}$, of the typical grain, where \bar{R}_t^{local} is random because the typical grain and its neighborhood are random. The exact definition of “local mean” is not important at this point. Essentially, we are interested in improving the prediction of \hat{R}_{t^+} from \hat{R}_t by taking \bar{R}_t^{local} into account. This means that the random vector

$$(\bar{R}_t^{\text{local}}, \hat{R}_t, \hat{R}_{t^+})$$

would be of interest. In that case, the random radius \hat{R}_{t^+} can depend on both \bar{R}_t^{local} and \hat{R}_t .

Instead, we consider the random vector

$$(\hat{R}_t/\bar{R}_t^{\text{local}}, \hat{R}_t/\bar{R}_t, \hat{R}_{t^+}/\bar{R}_{t^+}^{\text{local}}, \hat{R}_{t^+}/\bar{R}_{t^+}),$$

which yields essentially the same information, but has several advantages. First, we can assume that \bar{R}_t^{local} behaves similarly to the global mean \bar{R}_t . By considering the quotients of the typical grain radius and the two different normalizations, we can expect a dependence structure between the first two components with a very high correlation, which makes modeling easier. Second, the remaining two components are structured exactly in the same way. It is necessary to predict $\hat{R}_{t^+}/\bar{R}_{t^+}^{\text{local}}$, as well, because this information is required for the next time step, $t^+ \rightarrow t^{++} = t^+ + t_{\text{step}}$. Because $\hat{R}_{t^+}/\bar{R}_{t^+}$ and $\hat{R}_{t^+}/\bar{R}_{t^+}^{\text{local}}$ are predicted (and the global mean \bar{R}_{t^+} is deterministic and known), $\bar{R}_{t^+}^{\text{local}}$ is predicted implicitly.

Note that the definition of a local mean \bar{R}_t^{local} makes sense only as long as the typical grain is alive — *i.e.*, its radius \hat{R}_t is positive. If $\hat{R}_t = 0$, then we set $\hat{R}_t/\bar{R}_t^{\text{local}} = 0$ for consistency. As for the grain radius, we assume the distributions of $\{\bar{R}_t^{\text{local}}, t \in T_{\text{model}}\}$ to be self similar with respect to $\{\bar{R}_t, t \in T_{\text{model}}\}$.

In principle, the modeling approach is exactly the same for a four-dimensional random vector as discussed before in Sections 3.2 and 3.3 in the two-dimensional case. The marginal distributions are chosen individually, then a suitable copula must be selected. A disadvantage of the four-dimensional GSE model is that it

is harder to find a suitable 4D copula in comparison to the two-dimensional case. In particular, one challenge is that the two-dimensional marginal distribution of the last two components ($\hat{R}_{t^+}/\bar{R}_{t^+}^{\text{local}}$, $\hat{R}_{t^+}/\bar{R}_{t^+}$) describing the system at time t^+ must have exactly the same distribution as the two-dimensional marginal distribution of the first two components ($\hat{R}_{t^+}/\bar{R}_{t^+}^{\text{local}}$, $\hat{R}_{t^+}/\bar{R}_{t^+}$) in the next transition from t^+ to $t^{++} = t^+ + t_{\text{step}}$.

This must be guaranteed by a suitable choice of the copula. Unfortunately, this is not easy because standard copula families do not have this property (except the co-monotonicity copula, which is not useful in this case). However, it turns out that so-called vine copulas are very flexible — and a suitable vine copula construction that solves this problem is introduced in the following section.

3.5. Vine copula construction

First, we show how multivariate distributions can be described by a decomposition into bivariate distributions (and therefore, bivariate copulas). Then, we use this knowledge to construct a four-dimensional copula that has all properties as required for the GSE model introduced in Section 3.4.

Under the assumption that an m -dimensional random vector $X = (X_1, \dots, X_m)$ has the joint density $f : \mathbb{R}^m \rightarrow [0, \infty)$, it can be decomposed into

$$f(x_1, \dots, x_m) = f_1(x_1) f_{2|1}(x_2 | x_1) f_{3|1,2}(x_3 | x_1, x_2) \times f_{m|1, \dots, m-1}(x_m | x_1, \dots, x_{m-1}), \quad (5)$$

where f_1 is a short-hand notation for the density of X_1 , $f_{2|1}(\cdot | x_1)$ for the density of X_2 under the condition that $X_1 = x_1$, etc. The corresponding distribution functions are denoted by F_1 , $F_{2|1}$, etc. By applying Sklar's theorem (Appendix A) to the density of (X_1, X_2) it holds that

$$f_{1,2}(x_1, x_2) = c_{1,2}(F_1(x_1), F_2(x_2)) f_1(x_1) f_2(x_2)$$

where $c_{1,2}$ is the density of the copula $C_{1,2}$ of (X_1, X_2) , and $f_{2|1}(x_2 | x_1) = f_{2,1}(x_2, x_1)/f_1(x_1)$ can be rewritten as

$$f_{2|1}(x_2 | x_1) = c_{2,1}(F_2(x_2), F_1(x_1)) f_2(x_2). \quad (6)$$

(Note that the order of the components in the density can be changed together with the arguments, e.g., $f_{1,2}(x_1, x_2) = f_{2,1}(x_2, x_1)$ for all $x_1, x_2 \in \mathbb{R}$.) This procedure can be iterated to describe all conditional densities by bivariate copulas. For $m = 4$, one possible way to

rewrite the remaining conditional densities is

$$\begin{aligned} f_{3|1,2}(x_3 | x_1, x_2) &= c_{3,1|2}(F_{3|2}(x_3 | x_2), F_{1|2}(x_1 | x_2)) \\ &\quad \times f_{3|2}(x_3 | x_2) \\ &= c_{3,1|2}(F_{3|2}(x_3 | x_2), F_{1|2}(x_1 | x_2)) \\ &\quad \times c_{3,2}(F_3(x_3), F_2(x_2)) f_3(x_3) \end{aligned} \quad (7)$$

and

$$\begin{aligned} f_{4|1,2,3}(x_4 | x_1, x_2, x_3) &= c_{4,1|2,3}(F_{4|2,3}(x_4 | x_2, x_3), \\ &\quad F_{1|2,3}(x_1 | x_2, x_3)) \\ &\quad \times f_{4|2,3}(x_4 | x_2, x_3) \\ &= c_{4,1|2,3}(F_{4|2,3}(x_4 | x_2, x_3), \\ &\quad F_{1|2,3}(x_1 | x_2, x_3)) \\ &\quad \times c_{4,2|3}(F_{4|3}(x_4 | x_3), F_{2|3}(x_2 | x_3)) \\ &\quad \times c_{4,3}(F_4(x_4), F_3(x_3)) f_4(x_4). \end{aligned} \quad (8)$$

This decomposition works for all absolutely continuous distributions. However, note that in general the bivariate copulas (e.g., $c_{3,1|2}$) depend on the conditioning parameter vector (e.g., x_2). Usually, it is assumed that, e.g., $c_{3,1|2}$ does not depend on the value x_2 (in fact, for multivariate normal distributions, it can be shown that there is no such dependence, which makes this assumption more reasonable in the general case). This simplification is important in order to keep model selection fast and tractable [32]. Even with this constraint, this modeling approach is very flexible — a relatively small number of bivariate copulas can be combined to model high-dimensional and complex data, with good control over the dependencies.

In particular, the (absolutely continuous) random vector X can be chosen as a random vector with uniform marginals on $[0, 1]$ such that the distribution function F_X is exactly a copula (denoted as C). Then, for $m = 4$, the copula density function $c : [0, 1]^4 \rightarrow [0, \infty)$ can be given using bivariate copula densities $c_{1,2}$, $c_{2,3}$, $c_{3,4}$, $c_{1,3|2}$, $c_{2,4|3}$, and $c_{1,4|1,2}$, which are combined together as deduced in (5) to (8). Note that, in this case, the uniform marginal distributions imply $f_1(z) = 1$, $f_2(z) = 1$, $f_3(z) = 1$, $f_4(z) = 1$ for $z \in [0, 1]$. As a consequence, the copula density is given by

$$c(x_1, x_2, x_3, x_4) = c_{2,1} c_{3,1|2} c_{3,2} c_{4,1|2,3} c_{4,2|3} c_{4,3},$$

for $(x_1, x_2, x_3, x_4) \in [0, 1]^4$, where on the right-hand side all parameters of the functions (compare previous formulas) are left out to shorten the notation.

The representation of the four-dimensional copula density as described above is known in the literature as a D-vine copula (see, e.g., [32, 33]). An illustration of

Table 1: Ordinal sum copulas used as bivariate copulas for D-vine copula construction.

density	lower part copula	upper part copula	threshold
$c_{1,2}$	independence copula	Gaussian copula with correlation $\rho_{1,2}$	$h = q_t$
$c_{2,3}$	independence copula	Gaussian copula with correlation $\rho_{2,3}(t)$	$h = q_t$
$c_{3,4}$	independence copula	Gaussian copula with correlation $\rho_{3,4} = \rho_{1,2}$	$h = q_{t^+}$
$c_{1,3 2}$	independence copula	independence copula	$h = q_t$
$c_{2,4 3}$	independence copula	independence copula	$h = q_t$
$c_{1,4 1,2}$	independence copula	Gaussian copula with correlation $\rho_{1,4}(t)$	$h = q_t$

765 the hierarchical dependency structure is given in Figure 5. Note that the decomposition of the density is not unique — in general, other representations lead to regular vines, and the so-called D-vines are a special case.

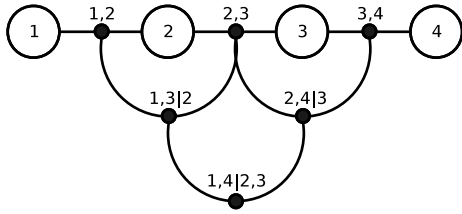


Figure 5: Schematic illustration of the hierarchical structure of the D-vine for the modeling of four-dimensional random vectors. The numbers in circles denote the components of the random vector, and the black dots correspond to bivariate copulas.

770 Now, consider again the four-dimensional random vector from Section 3.4. In order to describe its dependency structure with the decomposition introduced above, we consider the random vector with rearranged components

$$(\hat{R}_t/\bar{R}_t^{\text{local}}, \hat{R}_t/\bar{R}_t, \hat{R}_{t^+}/\bar{R}_{t^+}, \hat{R}_{t^+}/\bar{R}_{t^+}^{\text{local}}),$$

775 It follows from Sklar’s theorem that there exists a copula \tilde{C} , which can be understood as the distribution function of a random vector $U = (U_1, U_2, U_3, U_4)$, where all components are uniformly distributed on $[0, 1]$, and the relationship of the marginals is

$$\begin{aligned} \hat{R}_t/\bar{R}_t^{\text{local}} &= F_{\hat{R}_t/\bar{R}_t^{\text{local}}}^{-1}(U_1), & \hat{R}_t/\bar{R}_t &= F_{\hat{R}_t/\bar{R}_t}^{-1}(U_2), \\ \hat{R}_{t^+}/\bar{R}_{t^+} &= F_{\hat{R}_{t^+}/\bar{R}_{t^+}}^{-1}(U_3), & \hat{R}_{t^+}/\bar{R}_{t^+}^{\text{local}} &= F_{\hat{R}_{t^+}/\bar{R}_{t^+}^{\text{local}}}^{-1}(U_4), \end{aligned}$$

(equality of distributions).

785 With the assumption that \tilde{C} is absolutely continuous, the decomposition of the joint density of the random vector U as presented at the beginning of this section is possible. Therefore, the complexity is split up into bivariate copulas, which are easier to choose with regard to desired properties. One central requirement is that

790 if $\hat{R}_t = 0$, then all components of the four-dimensional random vector must be zero. Therefore, all bivariate copulas are chosen as ordinal sum copulas with a threshold value of at least q_t ; an overview is given in Table 1.

795 Furthermore, the first two components must always be simultaneously zero, and the same holds for the last two components (all with probability 1). This is ensured by choosing the thresholds as q_t and q_{t^+} for $c_{1,2}$ and $c_{3,4}$, respectively, which corresponds exactly to the proportion of grains with radius zero in the one-dimensional marginal distributions. For $c_{1,2}$, if $\hat{R}_t > 0$, then we are in the “upper part” copula. The choice of a Gaussian copula with correlation $\rho_{1,2}$ means that $(\hat{R}_t/\bar{R}_t^{\text{local}}, \hat{R}_t/\bar{R}_t | \hat{R}_t > 0) = (R_t/\bar{R}_t^{\text{local}}, R_t/\bar{R}_t)$ follows a Gaussian copula. The same construction with q_{t^+} is suitable for $c_{3,4}$, and the correlation $\rho_{3,4}$ must be equal to $\rho_{1,2}$ due to self-similarity of the non-dead grains.

800 The copula density $c_{2,3}$ describes the dependence structure of $(\hat{R}_t/\bar{R}_t, \hat{R}_{t^+}/\bar{R}_{t^+})$. Under the condition $\hat{R}_t > 0$, it is also modeled by a Gaussian copula, but with a time-dependent correlation $\rho_{2,3}(t)$. This dependency on time makes sense because the growth of the mean radius is nonlinear (*i.e.*, power-law growth).

805 The bivariate copulas that model the “direct” dependency of two random variables are now clear. The remaining conditional dependencies of the D-vine copula are chosen as follows. Both upper parts of $c_{1,3|2}$ and $c_{2,4|3}$ are chosen as independence copulas because there is no special reason to assume a specific kind of relationship. However, it is clearly sensible to assume that there is a relationship between $\hat{R}_t/\bar{R}_t^{\text{local}}$ and $\hat{R}_{t^+}/\bar{R}_{t^+}^{\text{local}}$ similar to \hat{R}_t/\bar{R}_t and $\hat{R}_{t^+}/\bar{R}_{t^+}$. Therefore, we choose the upper part of $c_{1,4|1,2}$ as the density of a Gaussian copula with correlation $\rho_{1,4}(t)$. As for $\rho_{2,3}(t)$, $\rho_{1,4}(t)$ is a function that returns the correlation as appropriate for the transition from t to t^+ . Note that although we did not impose a conditional dependency structure with $c_{1,3|2}$ (which influences the effect of $\hat{R}_t/\bar{R}_t^{\text{local}}$ on $\hat{R}_{t^+}/\bar{R}_{t^+}$), the remaining bivariate copulas do enforce a certain dependency structure between $\hat{R}_t/\bar{R}_t^{\text{local}}$ and $\hat{R}_{t^+}/\bar{R}_{t^+}$.

830 Note that the condition mentioned at the end of Section 3.4 regarding the two-dimensional marginals of the four-dimensional vectors is fulfilled. The two components $(\hat{R}_t/\bar{R}_t^{\text{local}}, \hat{R}_t/\bar{R}_t)$ of the transition from t to t^+ 880 agree with the first two components $(\hat{R}_{t^+}/\bar{R}_{t^+}^{\text{local}}, \hat{R}_{t^+}/\bar{R}_{t^+})$ in the next transition from t^+ to t^{++} . This is true because the bivariate copula $c_{3,4}$ for t to t^+ has exactly the same parameters as $c_{1,2}$ for t^+ to t^{++} . 885

The fitting procedure and the quality of fit of the GSE model will be discussed in the subsequent section.

840 4. Model fitting and evaluation

In this section, the four-dimensional GSE model as explained above is fitted to experimental data and its quality of fit is evaluated. 890

4.1. Fitting the GSE model to experimental data

845 We assume at this point that the parameters of the power-law growth parameters and the radius distribution of an experimental data set are already known. This is described in [28], and the results for the data considered here are briefly summarized in Appendix B. As 850 already mentioned in Section 3.2, there is a linear relationship between the seed point radii of the Laguerre tessellation used to approximate the microstructure and the volume-equivalent radii of generated cells. Therefore, the fitted distribution for seed point radii is used as the grain radius distribution, *i.e.*, $R_t \sim \mathcal{N}_+(c_\mu \bar{R}_t, c_\sigma^2 \bar{R}_t^2)$. 855

The definition of \bar{R}_t^{local} has yet to be specified. For the experimental data, we introduced and evaluated a weighted local mean, see Section 2.4. The same definition is used now. The local mean is computed from the radii of adjacent grains weighted by the square root of their contact area. We determined the distribution of $R_t/\bar{R}_t^{\text{local}}$ by generating realizations of the stochastic microstructure model for one point in time, evaluating the (weighted) local mean radii of all cells, and fitting a parametric distribution to the obtained data. Generated from the 3D microstructure model, the resulting parameterization is less error-prone than the experimental data. A mixture of two truncated normal distributions yields a good fit. (The proportion of the first normal distribution truncated to positive radii is $\alpha = 0.671$, and, correspondingly, $1 - \alpha$ for the second. The first normal distribution has parameters $\mu_1 = 0.968$, $\sigma_1 = 0.304$, the second $\mu_2 = 0.607$, $\sigma_2 = 0.209$.) 860 865 870

All remaining parameters are obtained from experimental data. These are the correlation coefficients $\rho_{1,2}$, $\rho_{2,3}(\cdot)$ and $\rho_{1,4}(\cdot)$. The scalar value $\rho_{1,2} = 0.9651$ is estimated from the complete aggregated data set of all pairs 875

of globally and locally normalized grain radii (using the sample correlation coefficient), whereas $\rho_{2,3}$ and $\rho_{1,4}$ are time-dependent. For every transition from t to t' for $t' > t$ (and t' not necessarily equal to t^+), the experimental grain trajectories are used to estimate the sample correlation coefficient. We assume that the correlation depends only on the relative expected radius evolution $z = \bar{R}_{t'}/\bar{R}_t$. A scatter plot of this ratio to the estimated correlations shows a nice relationship, see Figure 6. Non-linear regression using the regression function $\rho_{a,b,e} : [1, \infty) \rightarrow [0, 1]$ defined as

$$\rho_{a,b,e}(z) = \exp\left(-\left(\frac{z-1.0}{a-b/z}\right)^e\right)$$

with parameters $a > 0$, $b \in [0, a)$, $e > 0$ yields good fits — see Figure 6. Note that $\rho_{a,b,e}(1) = 1$, which makes sense for this kind of correlation function. The obtained parameter values are $a_{2,3} = 2.939$, $b_{2,3} = 2.0$, $e_{2,3} = 1.695$ for prediction of $\rho_{2,3}$, and $a_{1,4} = 2.103$, $b_{1,4} = 1.5$, $e_{1,4} = 1.626$ for $\rho_{1,4}$. The parameter b has been fixed manually in both cases to obtain a good fit for z -values near 1, which is important because we use these functions only to compute the correlations for transitions from t to t^+ — *i.e.*, the value $z_t = \bar{R}_{t^+}/\bar{R}_t$ is close to 1. Finally, we obtain 900

$$\begin{aligned} \rho_{2,3}(t) &= \rho_{a_{2,3}, b_{2,3}, e_{2,3}}(z_t), & t \geq 0, \\ \rho_{1,4}(t) &= \rho_{a_{1,4}, b_{1,4}, e_{1,4}}(z_t), & t \geq 0, \end{aligned}$$

with z_t as given above.

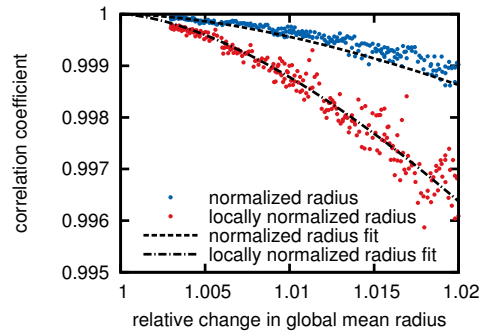
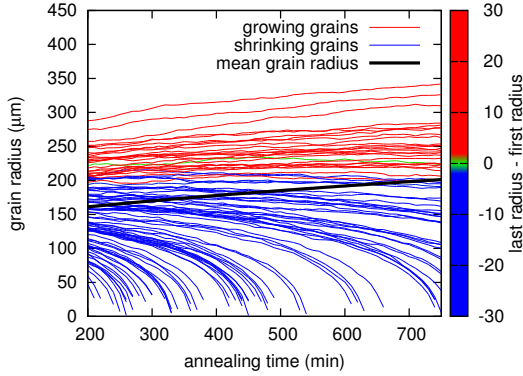


Figure 6: Empirical correlation coefficients computed from experimental tracks for grain radius transitions with global (blue) and local normalization (red). The corresponding regression curves are drawn in black.

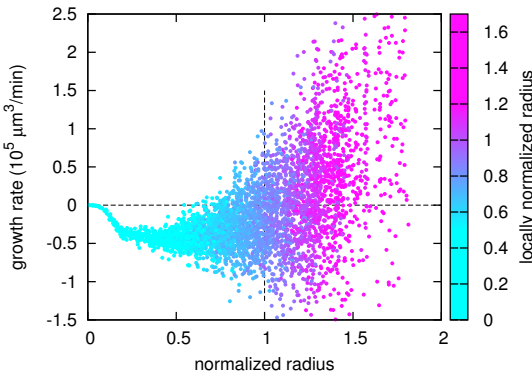
905 In practice, the sample correlation coefficients are not automatically good estimators for the parameters of bivariate Gaussian copulas in, *e.g.*, a D-vine construction. However, these coefficients are usually used as starting points for numerical optimization of the parameters in

910 maximum-likelihood fitting [33]. We refrain from carrying out such a complex fitting procedure because the 4D distribution already matches the original data nicely without further optimization.

4.2. Simulation results and discussion



(a) Size trajectories of simulated grains.



(b) Volumetric growth rates $4\pi r_t^2(r_{t^+} - r_t)/t_{\text{step}}$ obtained from grain radius transitions r_t to r_{t^+} in all simulated trajectories, for $t \in T_{\text{sim}}$ and $t^+ = t + t_{\text{step}} \in T_{\text{sim}}$. Colors indicate the values of locally normalized radii, *i.e.*, the grain radii relative to their respective local mean.

Figure 7: Simulation results for the fitted GSE model.

915 As in Sections 3.2 and 3.3, trajectories have been simulated. 100 trajectories are generated by the GSE model that was fitted to experimental data as described in Section 4.1. Figure 7 shows the trajectories and the growth rates of grains. A comparison to the experimental data in Figure 2 shows good qualitative agreement. 920 Note that in both cases there are grains having the same size whose trajectories evolve differently — *e.g.*, one is growing while the other is shrinking (Figures 2(a) and 7(a)). A comparison of Figures 2(b) and 7(b) reveals

925 that the overall transition behavior is quite similar; however, for larger grains, the volumetric growth rates manifest greater scatter in the simulated data than in experiment. This can be explained by properties of the Gaussian copula: The fluctuations in grain size, which are interpreted as noise, are the same in this model for all grain radii. However, for larger grains, a given change in radius has a greater effect on the volume than for smaller grains. One could improve the model fit in this regard by choosing another copula, for which the strength of the “noise” term is not the same for all grain sizes. 930

935 As a further step to evaluate the quality of fit, we compare grain trajectories including their local means. Figure 8 shows grain trajectories extracted from both experimental and simulated data. Note that experimental trajectories have been transformed to start from the same (relative) time point; that is, each trajectory is plotted against the value of $\bar{R}_{t'}/\bar{R}_t$ ($t' \geq t$) for the overall grain ensemble. (The same transformation is applied to simulated trajectories for a direct comparison.) Again, it can be observed that the simulated and experimental data agree qualitatively quite closely. The main apparent difference is that most experimental trajectories are incomplete (*i.e.*, shorter than the simulated trajectories). 940

945 From our analysis, we believe that the local mean is not the only quantity that influences individual grain evolution. Had this been the case, we would have expected a clearly visible relationship between growth rates and the locally normalized radius. The remaining randomness in the transitions is, in a sense, too large. Note that (seemingly) random behavior in real or numerically simulated systems has been discussed already in [5, 12, 44], where this phenomenon is called “locale noise”, “locale fluctuations” or “volume flux”. The fluctuations are larger for particles at or above the mean radius and for high volume fractions V_V , probably owing to stronger interactions with neighbors [5, 12, 44]. We think that the proposed modeling approach based on copulas is an excellent choice for investigating the dependency between other, yet-to-be-determined characteristics of the microstructure and the individual growth behavior of grains. 950 955 960 965

5. 4D microstructure model

In [28], we have described a 3D microstructure model for polycrystalline materials with a high volume fraction of the coarsening phase. A brief summary is given in Appendix B. Although this model can be used to simulate realistic 3D microstructures for arbitrary points in time, the dynamics of individual grains are not described. Therefore, we proposed the GSE model of Sec-

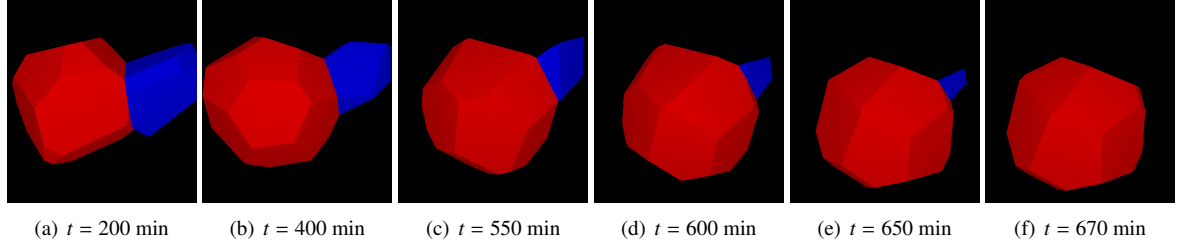


Figure 9: Evolution of the morphology of two adjacent grains, simulated by the 4D microstructure model. The red grain is growing, and the blue grain is shrinking — at first slowly, then faster, until it vanishes in the time interval (660, 670].

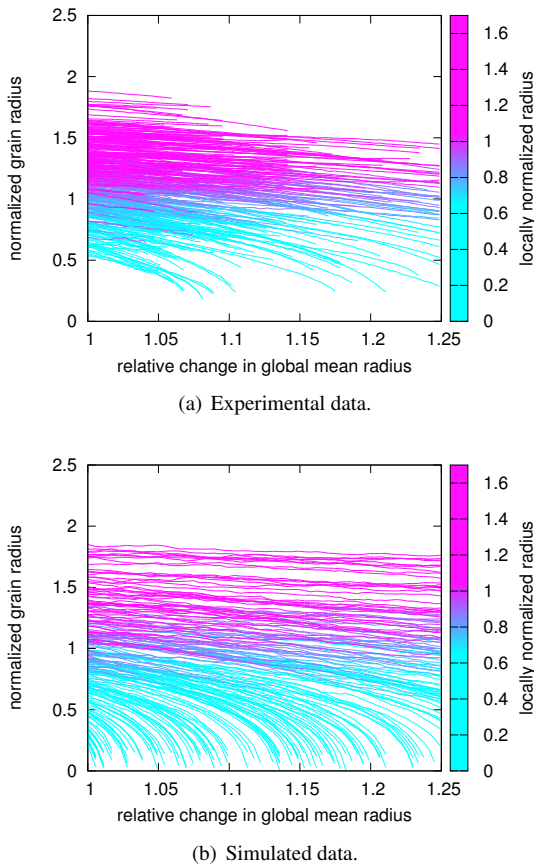


Figure 8: Comparison of size trajectories, for which grain radii are normalized to the global mean of their respective initial time point. A suitable normalization is performed for the time: it is transformed to the relative change in global mean radius. The colors of trajectories can vary over time as the locally normalized radius changes.

975 tion 3, which models the transition of a given grain to its next state using correlated random variables for the grain radii (but not considering the 3D shape of individual grains). In this section, these two models are combined to obtain a 4D microstructure model — *i.e.*, their

980 combination describes the possible evolution of a full 3D microstructure over time.

5.1. 3D model extension

985 Extension of the 3D microstructure model of Ref. [28] (Appendix B) to 4D with discrete time steps is straightforward. As before, we exploit the fact that the radii of seed points correspond almost exactly to the volume-equivalent radii of cells. Therefore, we always work directly on the radii belonging to seed points. The initial random microstructure in \mathbb{R}^3 is given by the stochastic microstructure model proposed in [28]. The transition for each seed point is performed by a two-step procedure. First, the GSE model is used to determine the radius evolution of each seed point; a new radius of zero means that the grain has died. Second, a non-overlapping set of hard cores is obtained by shifting the seed points appropriately based on collective-rearrangement (as described in [45] for an infinite number of spheres that are packed in \mathbb{R}^3). In this manner, each seed point position is updated implicitly. Note that the local mean of each grain can be evaluated, and this information is used to predict a new grain radius. The exact position and shape of the new grain is specified indirectly by the predicted seed points.

5.2. Simulation algorithm

1005 As in [28, Section 3.3], the simulation of the microstructure should be performed in a bounded simulation window $W \subset \mathbb{R}^3$. Required are the parameters of the 3D microstructure model and the GSE model (Section 3.4). The algorithm to obtain a series of microstructures for all time points $T_{\text{sim}} = \{t_{\text{min}}, t_{\text{min}} + t_{\text{step}}, \dots, t_{\text{max}}\}$ consists of 7 steps:

1. Define the plus sampling cuboid $W_+ \supset W$ and simulate the set of weighted seed points S_t in W_+ at time $t = t_{\text{min}}$ as given in [28, Section 3.3]. Note that a periodic boundary is used for the packing

of hard sphere cores in W_+ . The seed points are denoted by $S_t = \{(s_t(i), r_t(i)), i \in I\}$, where I is a suitable index set.

2. Set $I'_t = \{i \in I : r_t(i) > 0\}$ and $S'_t = \{(s_t(i), r_t(i)), i \in I'_t\}$. Compute the Laguerre tessellation $\{C_t(i), i \in I'_t\}$ with $C_t(i) = C((s_t(i), r_t(i)), S'_t)$ and a periodic boundary on the cuboid W_+ .

3. Set $t^+ = t + t_{\text{step}}$. Terminate if $t^+ \notin T_{\text{sim}}$.

4. Set up the GSE model

$$(\dot{R}_t/\bar{R}_t^{\text{local}}, \dot{R}_t/\bar{R}_t, \dot{R}_{t^+}/\bar{R}_{t^+}^{\text{local}}, \dot{R}_{t^+}/\bar{R}_{t^+}),$$

for a single transition from t to t^+ . It is convenient to assume that the time t is the first time step, *i.e.*, there are no dead grains and consequently $q_t = 0$, $q_{t^+} = 1 - \bar{R}_t^3/\bar{R}_{t^+}^3$.

5. For every grain $i \in I'_t$, compute the normalized radius $r_t(i)/\bar{R}_t$, the local mean $\bar{r}_t^{\text{local}}(i)$, and the locally normalized radius $r_t(i)/\bar{r}_t^{\text{local}}(i)$. Then, use the GSE model to obtain a realization of $\dot{R}_{t^+}/\bar{R}_{t^+}$ under the conditions $\dot{R}_t/\bar{R}_t = r_t(i)/\bar{R}_t$ and $\dot{R}_t/\bar{R}_t^{\text{local}} = r_t(i)/\bar{r}_t^{\text{local}}(i)$. This realization is denoted as $r_{t^+}(i)/\bar{R}_{t^+}$. For $i \notin I'_t$, set $r_{t^+}(i) = 0$.

6. An updated set of seed points with radii for time t^+ is now given by $\{(s_{t^+}(i), r_{t^+}(i)), i \in I\}$. These seed points have to be rearranged such that their hard cores are non-overlapping (as in step 1, respecting the constraint of periodic boundary conditions). The result is denoted by $S_{t^+} = \{(s_{t^+}(i), r_{t^+}(i)), i \in I\}$.

7. Set $t = t^+$ and go to step 2.

The algorithm described above yields a sequence of seed points $\{S_t : t \in T_{\text{sim}}\}$ and a sequence of tessellations $\{T_t : t \in T_{\text{sim}}\}$ with $T_t = \{C_t(i) : i \in I'_t \text{ and } C_t(i) \cap W \neq \emptyset\}$, *i.e.*, T_t consists of all cells for grains that are “alive” at time t and that also intersect W .

5.3. Simulation results and discussion

Figure 9 illustrates the simulated microstructure evolution of two adjacent grains. A growing grain was selected and a 3D visualization is shown together with a small neighbor that vanishes after some time. The evolution looks quite plausible, although it is difficult to evaluate its validity on a quantitative basis (beyond the investigations already performed in Section 4.2). Note that the evolution of individual grains is based on a statistical approach: any factors that influence growth but

are not implemented in the GSE model are modeled by random fluctuations, which are of course just that — random. Therefore, we do not expect deterministic local evolution — such as curvature-driven boundary migration — to be predicted perfectly; nevertheless, the local evolution is correct in a statistical sense when considering the overall ensemble of grains. Because the positions of grains are modeled implicitly for every transition in time, grains may “wobble” owing to changes in their own radius and that of their neighboring grains (which arise from the simulated noise term). Such artifacts could be suppressed by closer consideration (and integration) of relevant factors influencing the growth process.

6. Conclusions and outlook

In this paper, we use a parametric stochastic model to describe grain trajectories that were observed experimentally during Ostwald ripening. The proposed grain size evolution (GSE) model is a flexible stochastic approach that predicts the (non-deterministic) radius transition for a typical grain from one point in time to the next. The model is based on the representation of multivariate probability distributions by copulas. Our interest lies in taking local characteristics into account, *e.g.*, the grain neighborhood, when modeling the evolution of the size of the typical grain. Therefore, we investigated the influence of the local mean radius, which was expected to be relevant to the grain radius evolution; however, we found that the local mean radius is insufficient to account for all aspects of the grain growth observed in the experimental system.

Because the GSE model describes the radius evolution of the typical grain over time (whereby “typical” is not restricted to typical cases only, see footnote¹), the evolution of all grains in a system can be predicted individually. As an application, we extend our existing 3D microstructure model [28] to 4D using the GSE model. With this extension, an initial microstructure can be updated to reflect possible structural evolutions. The position and shape of grains is captured implicitly. The accuracy of such a prediction depends directly on the choice of “good” local characteristics as factors influencing the growth.

For this reason, the determination of relevant characteristics beyond the local mean radius is a possible next step toward improving the stochastic model. For example, the volume change entailed by physical models like, *e.g.*, [46] for grain growth could be included. Then, the stochastic model provides a possibility to assess the predictive power of the physical ansatz. To avoid problems

1110 with the processing of experimental data sets, we plan to
 use simulated microstructures and trajectories obtained,
 for example, from phase-field modeling. This offers the
 advantage of allowing one to investigate structural char-
 1115 acteristics that are difficult to extract from (noisy) exper-
 imental image data. With complete information on the
 evolution of the microstructure, we could then assess —
 and potentially improve upon — the choice of bivariate
 copulas in the vine construction.

Appendix A. Copulas

1120 A short introduction to the modeling of multivariate
 distributions by copulas is given in this section. Cop-
 ulas provide a flexible modeling approach (see, *e.g.*,
 [32, 33]), where a copula is an m -dimensional distri-
 bution function with uniform marginals on the interval
 1125 $[0, 1]$ for any fixed integer $m \geq 2$. As shown below, cop-
 ulas capture the dependencies between the components
 of random vectors.

Let $X = (X_1, \dots, X_m)$ be an m -dimensional ran-
 dom vector that has the multivariate distribution func-
 1130 tion $F_X(x_1, \dots, x_m) = \mathbb{P}(X_1 \leq x_1, \dots, X_m \leq x_m)$ and
 marginal distribution functions $F_{X_i}(x) = \mathbb{P}(X_i \leq x)$ for
 $i = 1, \dots, m$. Then, Sklar’s theorem [32, 33] states that
 there exists a copula $C : [0, 1]^m \rightarrow [0, 1]$ such that

$$F_X(x_1, \dots, x_m) = C(F_{X_1}(x_1), \dots, F_{X_m}(x_m)) \quad (\text{A.1}) \quad 1135$$

1135 for all $x_1, \dots, x_m \in \mathbb{R}$. Conversely, if an m -
 dimensional copula C and m one-dimensional distribu-
 tions F_{X_1}, \dots, F_{X_m} are given, then the function F_X de-
 fined in (A.1) is a multivariate distribution function.

Typically, one has observations of $X = (X_1, \dots, X_m)$
 1140 and the underlying multivariate distribution is unknown.
 In this case, the idea is to combine a (parametric) cop-
 ula C and m (parametric) one-dimensional distribution
 functions F_{X_1}, \dots, F_{X_m} to obtain a multivariate distri-
 bution function F_X by formula (A.1). Using the empirical
 1145 distribution functions $\hat{F}_{X_1}, \dots, \hat{F}_{X_m}$ of the marginals, the
 copula is fitted to $\hat{F}_{X_1}(X_1), \dots, \hat{F}_{X_m}(X_m)$ by a maximum-
 likelihood technique; this methodology is called semi-
 parametric pseudo-maximum likelihood [33, 47]. The
 univariate marginals are fitted separately using classical
 1150 maximum-likelihood techniques (see, *e.g.*, [48]).

There are a few basic and important types of copu-
 las. First, the independence copula (or product copula)
 is given by

$$C^\Pi(u_1, \dots, u_m) = u_1 \times \dots \times u_m, \quad 1155$$

1155 which means that a random vector (X_1, \dots, X_m) con-
 structed with this copula has independent components

X_1, \dots, X_m . The counterpart is a perfect linear dependence
 (*i.e.*, correlation of 1), which is obtained by the
 co-monotonicity copula defined by

$$C^+(u_1, \dots, u_m) = \min\{u_1, \dots, u_m\}.$$

Third, the multivariate normal distribution is a well-
 known and simple multivariate distribution. Its depen-
 dence structure is given by the so-called Gaussian cop-
 ula. Let $\Sigma \in \mathbb{R}^{m \times m}$ denote a correlation matrix (*i.e.*, a
 covariance matrix whose entries are all in the interval
 1160 $[-1, 1]$, and the diagonal entries of which are all equal
 to unity). Then, the Gaussian copula for the correlation
 matrix Σ is given by

$$C_\Sigma^{\text{Gauss}}(u_1, \dots, u_m) = \Phi_\Sigma(\Phi^{-1}(u_1), \dots, \Phi^{-1}(u_m)),$$

where Φ_Σ is the cumulative distribution function of a
 multivariate normal distribution with mean vector zero
 and correlation matrix Σ , and Φ^{-1} is the inverse cumu-
 lative distribution function of a (univariate) normal dis-
 tribution with expectation zero and variance 1.

In this paper, we also require the possibility to
 combine two copulas to form a new copula as il-
 lustrated in Figure A.10. This is a so-called ordinal
 sum of two copulas [49]. Let c_1 and c_2 denote
 the density functions of two absolutely continuous m -
 dimensional copulas C_1 and C_2 , *i.e.*, $C_i(u_1, \dots, u_m) =$
 $\int_{-\infty}^{u_1} \dots \int_{-\infty}^{u_m} c_i(\tilde{u}_1, \dots, \tilde{u}_m) d\tilde{u}_m \dots d\tilde{u}_1$, $i = 1, 2$, and let
 $h \in (0, 1)$. Then, we define the density $c : [0, 1]^m \rightarrow$
 $[0, \infty)$ of the ordinal sum copula C as

$$c(u_1, \dots, u_m) = \begin{cases} h c_1\left(\frac{u_1}{h}, \dots, \frac{u_m}{h}\right) & \text{if } (u_1, \dots, u_m) \in [0, h]^m, \\ (1-h) c_2\left(\frac{u_1-h}{1-h}, \dots, \frac{u_m-h}{1-h}\right) & \text{if } (u_1, \dots, u_m) \in (h, 1]^m, \\ 0 & \text{otherwise,} \end{cases}$$

1185 for $(u_1, \dots, u_m) \in [0, 1]^m$. The ordinal sum copula C
 can also be defined directly in an analogous way (this is
 required if C_1 or C_2 is not absolutely continuous); how-
 ever, the density is easier to interpret, *cf.* Figure A.10.
 In this paper, we call C_1 the “lower part” copula, and
 C_2 the “upper part” copula. It can be shown that the
 ordinal sum copula with density c agrees with the co-
 monotonicity copula C^+ in the unshaded regions of Fig-
 ure A.10. For, *e.g.*, a random vector $U = (U_1, U_2)$ with
 uniform marginals on $[0, 1]$ and ordinal sum copula, this
 1190 means that $U_1 \in [0, h]$ implies $U_2 \in [0, h]$ and vice versa
 (with probability 1), and this does not depend on C_1 or
 C_2 . The same holds for the range $[h, 1]$, of course.

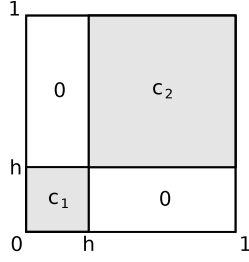


Figure A.10: Schematic illustration of (bivariate) ordinal sum copula density, which is constructed from two bivariate copulas that are scaled to “fit” into the two gray rectangles. The density in the white regions is zero, the threshold $h \in (0, 1)$ defines the transition point between the two copulas.

Appendix B. 3D microstructure model

In this section, the most important ideas and results from [28] are briefly summarized. First, the Laguerre tessellation is introduced, which is suitable for representing space-filling grain microstructures. The Laguerre tessellation uses so-called seed points to generate cells for grains. By selecting a random set of seed points, we obtain a random tessellation. This approach is used to construct a stochastic model for the 3D microstructure of polycrystalline materials, which is then fitted to experimental data.

Tessellations divide real space into cells, and, therefore, they are a natural choice for modeling polycrystalline data, for which grains fill space completely or almost completely. Each cell contains exactly one grain. The grains in our data set are nearly convex, which suggests the consideration of tessellation models with convex cells. A well-known tessellation model with convex cells is the Voronoi diagram [50]. In a Voronoi diagram, every point in space is assigned to its nearest seed point. A generalization is the Laguerre tessellation [50], which is similar to the Voronoi model but more flexible, owing to the introductions of an additional weight for each seed point.

Let $S = \{(s_i, r_i), i \in I\} \subset \mathbb{R}^3 \times \mathbb{R}_+$ denote a (locally finite) set of *seed points* s_i with positive weights r_i , where I is an index set. The *Laguerre cell* of (s_i, r_i) with respect to S is given by

$$C((s_i, r_i), S) = \{y \in \mathbb{R}^3 : |y - s_i|^2 - r_i^2 \leq |y - s_j|^2 - r_j^2, (s_j, r_j) \in S, j \neq i\}$$

The Laguerre tessellation is the family of all Laguerre cells $\{C((s_i, r_i), S), i \in I\}$. Note that every seed point (s_i, r_i) has a geometric interpretation — it can be understood as a sphere $B(s_i, r_i)$ centered at s_i with radius r_i . The weight r_i influences the resulting cell size.

The idea of the stochastic model in [28] is to deduce a random set of (weighted) seed points that generate close statistical agreement between the resulting Laguerre tessellation and a given experimental microstructure. A suitable procedure for determining such seed points is described in the following two paragraphs.

A random set of seed points results in moderately overlapping spheres. The radii of the spheres are assumed to follow a normal distribution truncated to the positive numbers — *i.e.*, $R_{\text{sphere}} \sim \mathcal{N}_+(\mu, \sigma^2)$. A hard core radius is assigned to each seed point by multiplying the original sphere radius by a factor $s_{\text{hc}} \in (0, 1]$. The set of hard cores is then rearranged by the application of a dense packing algorithm. The packing itself is based on a collective-rearrangement algorithm for spheres as described in [45], where the initial centers are simulated from a homogeneous Poisson process. Instead of the packing density d_{hc} of hard cores, the quantity $d = d_{\text{hc}}/s_{\text{hc}}^3$ is used as a parameter, which can be understood as the total volume of spheres divided by the volume of space into which they are packed. (Note that overlapping regions are counted more than once, and d can be greater than 1.) More details can be found in [28].

Because it is assumed that the modeled microstructures have the same statistical properties at all points in time (with only scaling factors varying over time), it makes sense to index the model parameters to the annealing time. In [28], this mapping is called the *time function*. The mean grain radius at time t is denoted by \bar{R}_t . The time function $p : \mathbb{R}_+ \rightarrow \mathbb{R}_+ \times \mathbb{R}_+ \times (0, 1] \times \mathbb{R}_+$ is given by

$$p(t) = \begin{pmatrix} \mu_t \\ \sigma_t^2 \\ s_{\text{hc}} \\ d \end{pmatrix} = \begin{pmatrix} c_\mu \bar{R}_t \\ (c_\sigma \bar{R}_t)^2 \\ s_{\text{hc}} \\ d \end{pmatrix},$$

with power-law growth of the mean grain radius

$$\bar{R}_t^n = \bar{R}_0^n + kt, \quad t > 0. \quad (\text{B.1})$$

Therefore, the parameters of the model are $c_\mu > 0$, $c_\sigma > 0$, $s_{\text{hc}} \in (0, 1]$, $d > 0$, $n > 0$, $k > 0$ and $\bar{R}_0 > 0$.

This model was fitted to experimental data in Ref. [28]. There, the parameters obtained for the power-law growth formula were $n = 3$, $k = 7197.3 \mu\text{m}^3/\text{min}$ and $\bar{R}_0 = 139.95 \mu\text{m}$. The remaining parameters were determined to be $c_\mu = 1.0$, $c_\sigma = 0.4$, $s_{\text{hc}} = 0.85$ and $d = 1.0$.

References

- [1] P. W. Voorhees, The theory of Ostwald ripening, *Journal of Statistical Physics* 38 (1985) 231–252.
- [2] P. W. Voorhees, Ostwald ripening of two-phase mixtures, *Annual Review of Materials Science* 22 (1992) 197–215.
- [3] L. Ratke, P. W. Voorhees, *Growth and Coarsening: Ostwald Ripening in Material Processing*, Springer, Heidelberg, 2002.
- [4] A. Baldan, Progress in Ostwald ripening theories and their applications to nickel-base superalloys - Part I: Ostwald ripening theories, *Journal of Materials Science* 37 (2002) 2171–2202.
- [5] K. G. Wang, M. E. Glicksman, K. Rajan, Length scales in phase coarsening: Theory, simulation, and experiment, *Computational Materials Science* 34 (3) (2005) 235–253.
- [6] K. G. Wang, M. E. Glicksman, *Ostwald Ripening in Materials Processing*, in: J. R. Groza, J. F. Shackelford, E. J. Lavernia, M. T. Powers (Eds.), *Materials Processing Handbook*, CRC Press, Boca Raton, 2007, pp. 5–1–5–20.
- [7] I. M. Lifshitz, V. V. Slyozov, The kinetics of precipitation from supersaturated solid solutions, *Journal of Physics and Chemistry of Solids* 19 (1–2) (1961) 35–50.
- [8] C. Wagner, Theorie der Alterung von Niederschlägen durch Umlösen (Ostwald-Reifung), *Zeitschrift für Elektrochemie* 65 (7) (1961) 581–591.
- [9] W. W. Mullins, The statistical self-similarity hypothesis in grain growth and particle coarsening, *Journal of Applied Physics* 59 (1986) 1341–1349.
- [10] P. W. Voorhees, M. E. Glicksman, Ostwald ripening during liquid phase sintering—Effect of volume fraction on coarsening kinetics, *Metallurgical Transactions A* 15 (6) (1984) 1081–1088.
- [11] N. Akaiwa, P. W. Voorhees, Late-stage phase separation: Dynamics, spatial correlations, and structure functions, *Physical Review E* 49 (1994) 3860–3880.
- [12] K. G. Wang, M. E. Glicksman, C. Lou, Correlations and fluctuations in phase coarsening, *Physical Review E* 73 (2006) 061502.
- [13] S. P. Marsh, M. E. Glicksman, Kinetics of phase coarsening in dense systems, *Acta Materialia* 44 (1996) 3761–3771.
- [14] S. P. Marsh, M. E. Glicksman, Ostwald ripening in non-spherical morphologies, *Materials Science and Engineering A* 238 (1) (1997) 140–147.
- [15] R. T. DeHoff, C. V. Iswaran, The usefulness of integral mean curvature measurements in the study of the kinetics of coarsening, *Metallurgical Transactions A* 13 (8) (1982) 1389–1395.
- [16] S. C. Hardy, P. W. Voorhees, Ostwald ripening in a system with a high volume fraction of coarsening phase, *Metallurgical and Materials Transactions A* 19 (1988) 2713–2721.
- [17] D. J. Rowenhorst, J. P. Kuang, K. Thornton, P. W. Voorhees, Three-dimensional analysis of particle coarsening in high volume fraction solid-liquid mixtures, *Acta Materialia* 54 (2006) 2027–2039.
- [18] N. Limodin, L. Salvo, M. Suéry, M. DiMichiel, In situ investigation by X-ray tomography of the overall and local microstructural changes occurring during partial remelting of an Al–15.8 wt.% Cu alloy, *Acta Materialia* 55 (2007) 3177–3191.
- [19] T. Werz, M. Baumann, U. Wolfram, C. E. Krill III, Particle tracking during Ostwald ripening using time-resolved laboratory X-ray microtomography, *Materials Characterization* 90 (2014) 185–195.
- [20] P. Streitenberger, Analytical description of phase coarsening at high volume fraction, *Acta Materialia* 61 (2013) 5026–5035.
- [21] J. Svoboda, F. D. Fischer, Generalization of the Lifshitz–Slyozov–Wagner coarsening theory to non-dilute multi-component systems, *Acta Materialia* 79 (2014) 304–314.
- [22] K. G. Wang, X. Ding, K. Chang, L. Q. Chen, Phase-field simulation of phase coarsening at ultrahigh volume fractions, *Journal of Applied Physics* 107 (2010) 061801.
- [23] S. G. Kim, Large-scale three-dimensional simulation of Ostwald ripening, *Acta Materialia* 55 (2007) 6513–6525.
- [24] D. Fan, S. P. Chen, L.-Q. Chen, P. W. Voorhees, Phase-field simulation of 2-D Ostwald ripening in the high volume fraction regime, *Acta Materialia* 50 (8) (2002) 1895–1907.
- [25] A. Luque, J. Aldazabal, J. M. Martínez-Esnaola, A. Martín-Meizoso, J. G. Sevillano, R. S. Farr, Diffusional Monte Carlo model of liquid-phase sintering, *Mathematics and Computers in Simulation* 81 (2011) 2564–2580.
- [26] M. K. Chen, P. W. Voorhees, The dynamics of transient Ostwald ripening, *Modelling and Simulation in Materials Science and Engineering* 1 (1993) 591–612.
- [27] V. A. Snyder, J. Alkemper, P. W. Voorhees, Transient Ostwald ripening and the disagreement between steady-state coarsening theory and experiment, *Acta Materialia* 49 (4) (2001) 699–709.
- [28] A. Spettl, R. Wimmer, T. Werz, M. Heinze, S. Odenbach, C. E. Krill III, V. Schmidt, Stochastic 3D modeling of Ostwald ripening at ultra-high volume fractions of the coarsening phase, *Modelling and Simulation in Materials Science and Engineering* 23 (6) (2015) 065001.
- [29] J. H. Panchal, S. R. Kalidindi, D. L. McDowell, Key computational modeling issues in Integrated Computational Materials Engineering, *Computer-Aided Design* 45 (1) (2013) 4–25.
- [30] S. Meyn, R. L. Tweedie, *Markov Chains and Stochastic Stability*, 2nd Edition, Cambridge University Press, Cambridge, 2009.
- [31] R. Kindermann, J. L. Snell, *Markov Random Fields and Their Applications*, American Mathematical Society, Providence, 1980.
- [32] J.-F. Mai, M. Scherer, *Simulating Copulas: Stochastic Models, Sampling Algorithms, and Applications*, Imperial College Press, Singapur, 2012.
- [33] H. Joe, *Dependence Modeling with Copulas*, CRC Press, Boca Raton, 2015.
- [34] S. N. Chiu, D. Stoyan, W. S. Kendall, J. Mecke, *Stochastic Geometry and its Applications*, 3rd Edition, J. Wiley & Sons, Chichester, 2013.
- [35] T. B. Massalski, *Binary Alloy Phase Diagrams - AlCu phase diagram*, 3rd Edition, Vol. 1, ASM, Providence, pp. 141–143, 1996.
- [36] A. Lyckegaard, G. Johnson, P. Tafforeau, Correction of ring artifacts in X-ray tomographic images, *International Journal of Tomography and Statistics* 18 (F11) (2011) 1–9.
- [37] S. Beucher, C. Lantuéjoul, Use of watersheds in contour detection, in: *Proceedings of the International Workshop on Image Processing, Real-Time Edge and Motion Detection/Estimation*, Rennes, France, 1979, pp. 2.1–2.12.
- [38] S. Beucher, F. Meyer, The morphological approach to segmentation: the watershed transformation, in: E. R. Dougherty (Ed.), *Mathematical Morphology in Image Processing*, Marcel Dekker, New York, 1993, pp. 433–481.
- [39] J. B. T. M. Roerdink, A. Meijster, The watershed transform: definitions, algorithms, and parallelization strategies, *Fundamenta Informaticae* 41 (2001) 187–228.
- [40] R. Beare, G. Lehmann, The watershed transform in ITK - discussion and new developments, *The Insight Journal*, Paper ID: 92.
- [41] P. Soille, *Morphological Image Analysis: Principles and Applications*, 2nd Edition, Springer, Berlin, 2004.
- [42] H. Rue, L. Held, *Gaussian Markov Random Fields: Theory and Applications*, Chapman & Hall/CRC, Boca Raton, 2005.
- [43] S. Z. Li, *Markov Random Field Modeling in Image Analysis*, 3rd Edition, Springer, London, 2009.
- [44] M. E. Glicksman, K. G. Wang, S. P. Marsh, Stochastic effects in microstructure, *Journal of Materials Research* 5 (3) (2002) 231–

- 1405 241.
- [45] C. Hirsch, G. Gaiselmann, V. Schmidt, Asymptotic properties of collective-rearrangement algorithms, *ESAIM: Probability and Statistics* 19 (2015) 236–250.
- 1410 [46] R. D. MacPherson, D. J. Srolovitz, The von Neumann relation generalized to coarsening of three-dimensional microstructures, *Nature* 446 (2007) 1053–1055.
- [47] D. Ruppert, D. S. Matteson, *Statistics and Data Analysis for Financial Engineering*, 2nd Edition, Springer, New York, 2015.
- 1415 [48] G. Casella, R.-L. Berger, *Statistical Inference*, 2nd Edition, Duxbury, Pacific Grove, 2002.
- [49] R. B. Nelsen, *An Introduction to Copulas*, Springer, New York, 2006.
- 1420 [50] A. Okabe, B. Boots, K. Sugihara, S. N. Chiu, *Spatial Tesselations: Concepts and Applications of Voronoi Diagrams*, 2nd Edition, J. Wiley & Sons, Chichester, 2000.